Volume 12 | Number 13 | 7 July 2025

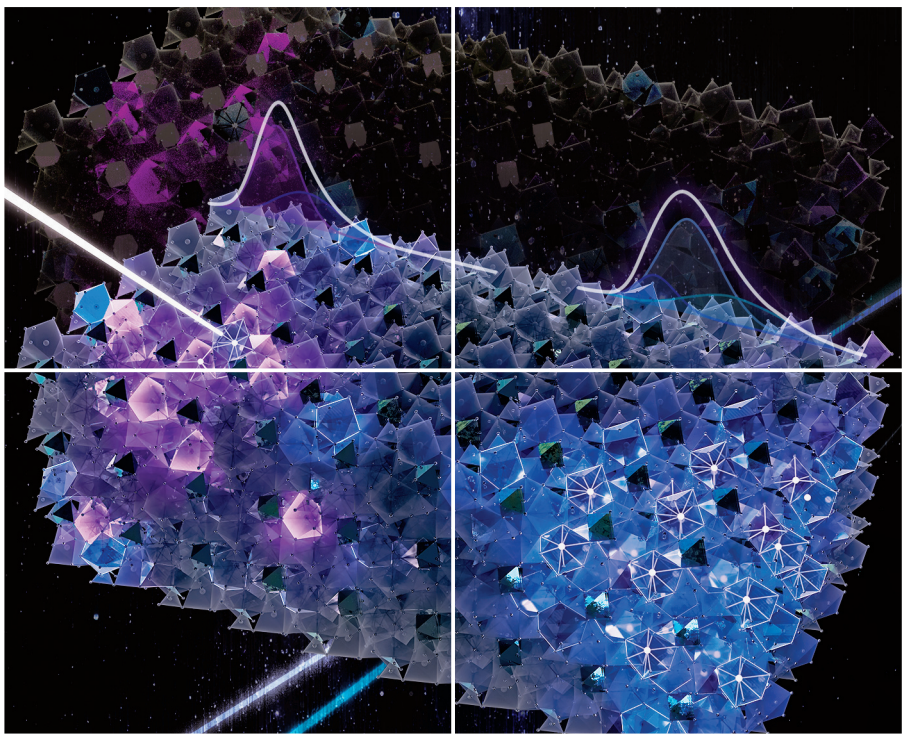

INORGANIC CHEMISTRY

FRONTIERS

CCS 中国化学会 CHINESE CHEMICAL SOCIETY

PEKING UNIVERSITY 1898

ROYAL SOCIETY OF CHEMISTRY

rsc.li/frontiers-inorganic

INORGANIC CHEMISTRY FRONTIERS

RESEARCH ARTICLE

View Article Online
View Journal | View Issue

Cite this: *Inorg. Chem. Front.*, 2025, **12**, 4186

Modulating optical properties through cation substitution: composition-property relationships in $M^{I}_{3}M^{III}P_3O_9N:Eu^{2+}$ (M^{I} = Na, K; M^{III} = Al, Ga, In)†

Nakyung Lee, [a,b] Justyna Zeler, [c] Małgorzata Sójka, [a,b] Eugeniusz Zych [c] and Jakoah Brgoch *[a,b]

Developing phosphors with narrow photoluminescence emission peaks and high chromatic stability holds significant importance in light-emitting diode (LED) display technologies, where a wide color gamut is essential to achieve the Rec. 2020 specifications. This research focuses on the optical properties of a solid solution: $M^{I}_{2.97}Eu_{0.015}M^{III}P_3O_9N$ [M^{I} = Na, K; M^{III} = Al, ($Al_{0.75}Ga_{0.25}$), ($Al_{0.5}Ga_{0.5}$), ($Al_{0.25}Ga_{0.75}$), Ga, ($Ga_{0.75}In_{0.25}$), ($Ga_{0.5}In_{0.5}$)] to understand how the narrow-emitting photoluminescence in $K_3AlP_3O_9N:Eu^{2+}$ can evolve during host structure cation substitution. Photoluminescence measurements at low temperature (15 K) support that Eu^{2+} replaces three crystallographically independent Na^{+} sites in $Na_{2.97}Eu_{0.015}AlP_3O_9N$, similar to the parent K^{+} phosphor, but substituting Ga^{3+} and In^{3+} for Al^{3+} leads to a change in Eu^{2+} site preference, narrowing the full-width-at-half-maximum (fwhm) of the emission peak. The chromatic stability and photoluminescence quantum yield are also enhanced with higher Ga^{3+} content in the host but not with In^{3+}. Thermoluminescence analysis indicates the relationship between trap states and the enhanced quantum yield with Ga^{3+} leads to the series' best performance. The analysis of the $M^{I}_{2.97}Eu_{0.015}M^{III}P_3O_9N$ series offers insight into the potential method for modulating optical properties with cation substitution in the host structure.

Received 10th February 2025,
Accepted 20th April 2025

DOI: 10.1039/d5qi00410a

rsc.li/frontiers-inorganic

1. Introduction

Pursuing sustainable alternatives to traditional lighting and more portable display technologies has led to the rapid development of phosphor-converted light-emitting diodes (pc-LEDs). Their energy efficiency and prolonged operating lifespan guarantee a reduction in electricity consumption and promise a substantial decrease in their environmental footprint.[1,2] Pc-LEDs generate white light by coating a blue LED (λ_{ex} = 450 nm) with yellow and red phosphors, which absorb the blue emission and down-shift it into a broad spectrum.[3,4] Alternatively, a combination of near-ultraviolet (n-UV) LED chips (λ_{ex} = 380 nm–420 nm) and blue, green, and red-emitting phosphors is another proposed strategy capable of generating higher-quality white light by covering a more significant portion of the visible spectrum. An added advantage of this approach is regulating the amount of blue LED light produced by the device in what is being called "human-centric" lighting.[5,6] Avoiding excessive exposure to blue light, which suppresses melatonin production and stimulates the brain, and replicating color temperature shifts throughout the day is valuable for regulating the human circadian rhythm. LED lighting can address these issues, provided phosphor conversion materials can be developed.

The U.S. Department of Energy has previously outlined the criteria for developing commercial-ready phosphors capable of generating white light.[7] Phosphors must be capable of absorbing and efficiently down-shifted light from blue or violet LEDs and produce narrow photoluminescence emission with a full-width-at-half-maximum (fwhm) that is ≈30 nm (red = 794 cm^{-1}, green = 1148 cm^{-1}, blue = 1485 cm^{-1}). The narrow emission is vital to enhance lighting efficacy by minimizing the emission of photons in the near-IR and UV regions. It is also crucial for display applications to generate a wider color gamut and achieve the Rec. 2020 specifications.[8–10] Commercially relevant phosphors should also withstand average LED operating temperatures of 150 °C without succumbing to thermally induced changes in the optical properties. For instance, a phosphor's emission intensity should change by less than 50% (ideally less than 4%) from room temperature up to 150 °C to overcome thermal quenching.[11] The phosphor's emission color

[a]*Department of Chemistry, University of Houston, Houston, Texas 77204, USA. E-mail: jbrgoch@uh.edu*
[b]*Texas Center for Superconductivity, University of Houston, Houston, Texas 77204, USA*
[c]*Faculty of Chemistry, University of Wroclaw, 14. F Joliot Curie Street, 50-383 Wroclaw, Poland*

† Electronic supplementary information (ESI) available. See DOI: https://doi.org/10.1039/d5qi00410a

must also not vary as a function of temperature shifting by less than a 3-step MacAdam ellipse.[12]

Given such specific requirements, new materials are constantly being tested. (Oxy-)nitrides substituted with rare-earth (RE) activator ions, like Eu^{2+}, are one major class of phosphors studied today motivated by their propensity to strongly absorb violet/blue light and re-emit these photons across the broad visible spectrum *via* the parity-allowed $4f^7 \leftrightarrow 4f^6 5d^1$ electronic transitions.[8,13,14] The energy position of these Eu^{2+} transitions is set based on the nature of the host structure's coordinating atoms and the geometry of the crystallographic substitution site. The resulting nephelauxetic effect stabilizes (lowers) the rare-earth 5d orbitals in energy by reducing the inter-electron repulsion of activator ions.[15–17] This effect depends mainly on the anion type, with N^{3-} causing a more considerable decrease in energy than O^{2-}, while O^{2-} is more effective than F^-. The 5d orbitals of the lanthanide ion are further separated by crystal field splitting (CFS) effects, which depend primarily on the coordination number, volume of the cation site, and symmetry of the site.[18,19] The combination of effects is exemplified by comparing the phosphorus oxynitride $Ba_2PO_3N:Eu^{2+}$ with the $[BaO_7N_3]$ and $[BaO_7N_2]$ sites generating cyan emission (λ_{em} = 530 nm), whereas the phosphate $Ba_2P_2O_7:Eu^{2+}$ shows blue-shifted emission (λ_{em} = 420 nm) from the $[BaO_{10}]$ and $[BaO_7]$ sites.[20,21]

The position of the electronic transitions and associated emission color is not necessarily binary. Forming a solid solution through meticulous elemental substitution is one approach that enables tuning of the phosphors' photoluminescent properties.[2,22,23] These substitutions are valuable on either the anion or the cation sublattice. The most common is varying the cation composition to change the properties gradually. For example, the $Rb_2(Ca_{1-x}Sr_x)P_2O_7:Eu^{2+}$ system replaces the larger cation Sr^{2+}($r_{6\text{-coord}}$ = 1.18 Å) for the smaller Ca^{2+}($r_{6\text{-coord}}$ = 1.00 Å) expanding the unit-cell, generating a continuous blue-shifted emission from 612 nm to 567 nm.[24] Similarly, oxynitrides can also benefit from forming solid solutions, provided cation charge compensation mechanisms are available. The oxynitridosilicate $Sr_{2-x}La_xSiO_{4-x}N_x$ solid solution incorporates nitrogen with the cation charge balanced out by adding La^{3+} for Sr^{2+}, resulting in a tunable red-shifted emission from 550 nm to 700 nm with increasing N^{3-} content.[25] Varying the composition does not just shift the maximum of the emission peak, but it can holistically impact the optical properties. In the $La_5(Si_{2+x}B_{1-x})(O_{13-x}N_x):Ce^{3+}$ system, the increase of N^{3-} shifts the emission from violet (λ_{em} = 421 nm) to blue (λ_{em} = 463 nm) region while simultaneously enhancing the thermal quenching temperature (T_{50}) from 120 °C (x = 0) to 202 °C (x = 0.7).[22] Solid solution formation can also create more complex outcomes like changing rare-earth substitution site preference in the phosphor. The $(Rb_{1-x}K_x)_2CaPO_4F:Eu^{2+}$ solid solution shows that decreasing the Rb^+ site volume while expanding the Ca^{2+} site by incorporating K^+ can cause significant changes by varying substitution site preference.[26] The pure Rb^+ composition shows strong site preference on $[Rb(2)O_8F_2]$ and no emission from $[CaO_4F_2]$, whereas $RbKCaPO_4F:Eu^{2+}$ shows a stronger emission peak from $[Rb(1)O_8F_2]$. Finally, a higher K^+ ratio than Rb^+ pushes the emission red-shifted by letting Eu^{2+} mostly occupy $[CaO_4F_2]$ sites than other Rb^+ sites. The study of solid solutions plays a crucial role in controlling the optical properties of phosphors.

One oxynitride discovered by our group where solid solutions may prove interesting for tuning the optical properties is the $K_3AlP_3O_9N:Eu^{2+}$ system.[27] This material's narrow emission (fwhm = 45 nm, 2110 cm^{-1}) and reasonable photoluminescent quantum yield (PLQY) of 60(4)%, holding promise in violet excited human-centric display concepts. Based on this previous study, the complete cation substitution of K^+ with a smaller Na^+ is tested to tune the emission color and investigate the influence of M^I site substitution on the optical properties. Subsequent investigations into solid solution substitutions on the M^{III} site following $Na_{2.97}Eu_{0.015}M^{III}P_3O_9N$ [M^{III} = Al, ($Al_{0.75}Ga_{0.25}$), ($Al_{0.5}Ga_{0.5}$), ($Al_{0.25}Ga_{0.75}$), Ga, ($Ga_{0.75}In_{0.25}$), ($Ga_{0.5}In_{0.5}$)] are performed to understand the chemistry of these Na^+ analogs in depth. The properties are investigated using low-temperature emission, temperature-dependent emission, and thermoluminescence (TL) glow curve measurements. These results highlight the impact of elemental substitution on optical properties and provide guidance for designing materials with a narrow emission peak. Although the resulting phosphors studied here are only excitable by UV light, the insights gained support the future development of advanced pc-LED phosphors.

2. Experimental procedure

2.1. Materials synthesis

The solid solutions of $(Na_{1-2x}Eu_x)_3AlP_3O_9N$ (x = 0.001, 0.0025, 0.005, 0.01, 0.02) and $Na_{2.97}Eu_{0.015}M^{III}P_3O_9N$ [M^{III} = Al, ($Al_{0.75}Ga_{0.25}$), ($Al_{0.5}Ga_{0.5}$), ($Al_{0.25}Ga_{0.75}$), Ga, ($Ga_{0.75}In_{0.25}$), ($Ga_{0.5}In_{0.5}$)] were synthesized by solid-state reactions starting from KPO_3, $Na_6[(PO_3)_6]$ (Sigma-Aldrich, 96%), Al_2O_3 (Alfa Aesar, 99%), Ga_2O_3 (Alfa Aesar, 99.99%), In_2O_3 (Alfa Aesar, 99.9%), and Eu_2O_3 (Alfa Aesar, 99.99%). KPO_3 was prepared by dehydrating KH_2PO_4 (Alfa Aesar, 99.0%) at 350 °C for 12 h in air. Each component was weighed out in the appropriate stoichiometric ratio, and the starting reagents were mixed and ground in an agate mortar and pestle using acetone as a wetting medium. Powders were further milled for 30 min in a high-energy ball mill (Spex 800 M Mixer/Mill) using polystyrene vials. The mixtures were then pressed into a 6 mm diameter pellet and placed on a bed of sacrificial powder in a boron nitride crucible. The pellets were heated at 800 °C for 12 hours under flowing NH_3 gas, with heating and cooling rates of 3 °C min^{-1}, to facilitate the *in situ* nitridation of the host structure and the reduction of Eu^{2+}.

2.2. Structural studies, density functional theory, and optical characterization

Powder X-ray diffractograms of all products were collected using an X'Pert PANalytical Empyrean 3 equipped with Cu Kα

(λ = 1.5406 Å) as the radiation source. Le Bail refinements were performed using the General Structural Analysis System II (GSAS-II) software.[28] The background was described using a Chebyshev-1 function, and the peak shapes were modeled by a pseudo-Voigt function. Scanning electron microscopy (SEM) micrographs and energy-dispersive X-ray spectroscopy (EDS) elemental mappings were collected using a Phenom Pharos scanning electron microscope attached with a 25 mm^2 silicon drift detector energy-dispersive X-ray spectrometer (Thermo Fisher Scientific). An accelerating voltage of 15 kV and an emission current of 12 μA were used.

The electronic bandgaps of the $Na_3M^{III}P_3O_9N$ (M^{III} = Al, $Al_{0.5}Ga_{0.5}$, Ga, $Ga_{0.5}In_{0.5}$) host structures were calculated using density functional theory (DFT). The calculations employed the Vienna *ab initio* simulation (VASP) package within the projector-augmented wave (PAW) method.[29,30] Structural optimization was first performed with exchange and correlation treated using the generalized gradient approximation (GGA) Perdew–Burke–Ernzerhof (PBE) functional.[31] The calculations employed a plane wave energy cut-off of 500 eV, as well as force and energy convergence criteria of 1×10^{-8} eV and 0.01 eV $Å^{-1}$, respectively, and an 8 × 8 × 8 Gamma-centered *k*-point grid.[32] The solid solutions (M^{III} = $Al_{0.5}Ga_{0.5}$, $Ga_{0.5}In_{0.5}$) were approximated using a 1 × 1 × 1 "supercell" with the M^{III} atoms decorated among the single crystallographic site with all possible permutations structurally optimized and the lowest energy structure selected for subsequent band gap and band structure calculations. A hybrid exchange and correlation functional (HSE06) with similar cut-off energy and energy convergence criteria but a 4 × 4 × 4 Gamma-centered *k*-point grid was used for these calculations.[33] The band structure and density of states plots are provided in Fig. S1.†

Steady-state photoluminescence and quantum yield measurements involved mixing the polycrystalline products in an optically transparent silicon epoxy (United Adhesives Inc., OP 4036) and depositing the combination onto a quartz slide (Chemglass). The excitation and emission spectra were obtained using a PTI fluorescence spectrophotometer equipped with a 75 W xenon arc lamp excitation source. The PLQY was determined following the method of de Mello *et al.*[34] using a Spectralon-coated integrating sphere (150 mm diameter, Labsphere) with an excitation wavelength of 340 nm. Temperature-dependent photoluminescence was recorded between 15 K and 600 K using a FLS1000 Fluorescence Spectrometer from Edinburgh Instruments Ltd. The samples were mounted on a copper holder in a closed-cycle helium cryostat from Lake Shore Cryotronics, using Silver Adhesive 503 glue from Electron Microscopy Sciences. A 450 W continuous xenon arc lamp was used as the excitation source for these measurements. A TMS302-X double grating excitation and emission monochromators with 2 × 325 mm focal lengths were used, and the luminescence signal was recorded with a Hamamatsu R928P high-gain photomultiplier detector thermoelectrically cooled to −22 °C. The excitation spectra were corrected for the incident light intensity, and the emission ones were corrected for the emission channel spectral sensitivity.

Thermoluminescence (TL) experiments were performed using Lexsyg Research Fully Automated TL/OSL Reader from Freiberg Instruments GmbH. An X-ray lamp VF-50J RTG with W-anode operated under 12 kV and 0.1 mA was used as a charging source. The phosphor samples' irradiation with X-rays (12 kV, 0.1 mA) was performed for 10 seconds, and then TL glow curves were recorded using a 9235QB-type photomultiplier from ET Enterprises in the range from 303 K to 773 K. All experiments were controlled through LexStudio 2 software.

3. Results and discussion

3.1. Distinctive optical behavior in $M^I_{2.97}Eu_{0.015}AlP_3O_9N$ (M^I = Na, K)

The previously reported phosphor, $K_3AlP_3O_9N:Eu^{2+}$, crystallizes in cubic space group $P2_13$ (No. 198), and is part of a broader isostructural series following $M^I_3M^{III}P_3O_9N$ (M^I = Na; K, M^{III} = Al; Ga; Cr; Fe; Mn).[36] Illustrated in Fig. 1a, the crystal structure was originally solved by single-crystal X-ray diffraction with three [PO_3N] tetrahedra connected through a nitrogen-occupied vertex that creates a [$N(PO_3)_3$] unit. The [AlO_6] octahedra share an O atom from six different [PO_3N] tetrahedra, producing an Al[$N(PO_3)_3$] backbone. There are three crystallographically independent M^I sites in the crystal structure: [$M^I(1)O_9$], [$M^I(2)O_6N$], and [$M^I(3)O_6$]. Although the [$M^I(1)O_9$] site was reported as a six-coordinated site in the original reference, a closer re-analysis suggests a nine-coordinated environment as a better description based on the bond lengths of the adjacent atoms and space-filling in the unit cell.[27]

The previous $K_3AlP_3O_9N:Eu^{2+}$ study showed a 454 nm (blue) emission at room temperature with a bandwidth of 45 nm (2110 cm^{-1}) under 400 nm excitation. The relatively narrow photoluminescence stemmed from two factors: site-selective excitation (λ_{ex} = 405 nm) efficiently removes the emission from [$K(1)O_9$], and a preferential thermal quenching of the [$K(3)O_6$] site at room temperature. As a result, only Eu^{2+} on the [$K(2)O_6N$] site contributes to the emission under violet excitation. Building on this prior investigation, this work first explores the substitution of K^+ with the smaller Na^+ ions (K^+: $r_{6\text{-coord}}$ = 1.38 Å, $r_{7\text{-coord}}$ = 1.46 Å, $r_{9\text{-coord}}$ = 1.55 Å; Na^+: $r_{6\text{-coord}}$ = 1.02 Å, $r_{7\text{-coord}}$ = 1.12 Å, $r_{9\text{-coord}}$ = 1.24 Å)[37] to understand the relationship between composition and the effects of cation substitution while tuning the emission color.

The reported synthesis of $Na_3AlP_3O_9N$ used a synthesis temperature of 800 °C with AlN in a molten flow of sodium polyphosphates.[38,39] In the study here, polycrystalline samples of $(Na_{1-2x}Eu_x)_3AlP_3O_9N$ (x = 0.001, 0.0025, 0.005, 0.01, 0.02) were obtained at 800 °C under flowing NH_3, which is used for supplying nitrogen in the target compositions and for reducing Eu^{3+} to Eu^{2+}. The products had no notable impurities, and their peaks matched the reference pattern, as confirmed by powder X-ray diffraction (Fig. S2a†). Analyzing the unit-cell dimensions using Le Bail refinements shows that the lattice parameters increase with the substitution of the larger Eu^{2+} ion for the smaller Na^+ ion ($Eu^{2+}r_{6\text{-coord}}$ = 1.17 Å, $r_{7\text{-coord}}$ =

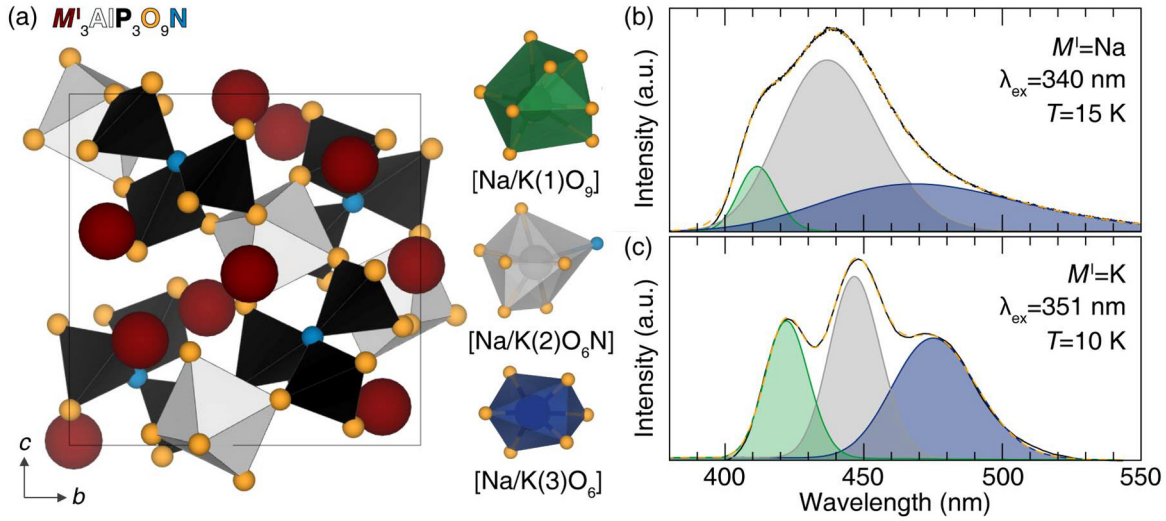

Fig. 1 (a) Crystal structure of $M^I_3AlP_3O_9N$ (ICSD #78373) and three crystallographically independent Na^+/K^+ sites for Eu^{2+} substitution. A bond length of <2.96 Å creates a $[M^I(1)O_6]$ polyhedron that is severely elongated and distorted. However, when the bond length is ≈2.98 Å, a 9-coordinated polyhedron $[M^I(1)O_9]$ creates a more reasonable site geometry in the unit cell that is more coherent with the photoluminescent characteristics. Photoluminescence deconvoluted emission spectrum of (b) $Na_{2.97}Eu_{0.015}AlP_3O_9N$ and (c) $K_{2.97}Eu_{0.015}AlP_3O_9N$ at low temperatures. Gaussian deconvolution was made by first converting the spectra into energy scale by means of Jacobian transformation.[35]

1.2 Å, $r_{9\text{-coord}}$ = 1.3 Å) (Fig. S2b†). The refined lattice parameters are provided in Table S1.†

Substituting Eu^{2+} into the solid solution $(Na_{1-2x}Eu_x)_3AlP_3O_9N$ generates deep blue luminescence with an excitation band ranging from 280 nm to 400 nm (see Fig. S2c†). The excitation spectra for x = 0.001, 0.0025, and 0.005 show little change in shape; however, a distinct shoulder appears around 375 nm in the excitation spectrum for x = 0.01 and 0.02. A similar trend is observed when collecting the emission spectrum using λ_{ex} = 340 nm, with a shoulder extending from 450 nm to 550 nm. As a result, there is a slight red shift in the deep blue emission, with $\lambda_{em,max}$ = 427 nm at x = 0.001 shifting to $\lambda_{em,max}$ = 432 nm at x = 0.02 as the concentration of Eu^{2+} increases. Generally, a higher concentration of larger Eu^{2+} ions expands the unit cell and the volume of the substituted sites, leading to a blue shift in the $\lambda_{em,max}$ position accompanied by lower crystal field splitting (CFS). However, in this case, the presence of shoulders in both photoluminescent excitation and emission spectra suggests that Eu^{2+} prefers to substitute onto $[Na(2)O_6N]$ or $[Na(3)O_6]$, resulting in a longer emission peak wavelength at higher rare earth concentrations.

The optimal Eu^{2+} concentration in the $(Na_{1-2x}Eu_x)_3AlP_3O_9N$ series was determined by measuring the PLQY under 340 nm excitation (Fig. S2d†). At x = 0.005, PLQY reaches the highest value among the series with 21(2) %. Beyond x = 0.01, the PLQY drops rapidly due to the increased probability of the energy transfer between Eu^{2+} ions. In higher Eu^{2+} concentrations, there is less separation between Eu^{2+} ions, increasing the likelihood of energy transfer and enabling electrons to find quenching sites, inducing a non-radiative relaxation. The critical distance of energy migration, R_c, between two activators can be calculated with eqn (1),

$$R_c = 2\left(\frac{3V}{4\pi x_c n}\right)^{1/3} \quad (1)$$

where V is the volume of the unit cell, x_c is the critical concentration of the activator at maximum emission intensity, and n is the sum of the Wyckoff positions of the crystallographically independent substitution sites.[40] The calculated R_c here is 26.2 Å. The long-distance non-radiative energy transfer generally occurs through electron exchange interaction or electric multipolar interaction. To decide what type of interaction among dipole–dipole (d–d), dipole–quaternary (d–q), and quaternary–quaternary (q–q) interactions causes the quenching, the emission intensity (I) at each activator concentration is analyzed with eqn (2),

$$\frac{I}{x} = k[1 + \beta(x)^{\theta/3}]^{-1} \quad (2)$$

where x is the activator concentration above the critical concentration, k and β are constants of a given host, and θ is the electric multipolar character.[41] The energy transfer mode of electric multipolar interaction can be confirmed by the values of θ = 6, 8, and 10, which correspond to d–d, d–q, and q–q interaction, respectively. With an assumption of $\beta(x)^{\theta/3} \gg 1$, eqn (2) can be simplified as a linear equation with slope $-\theta/3$.

$$\log I/x = k' - \theta/3 \log x (k' = \log k - \log \beta) \quad (3)$$

The plot of $\log I/x$ *versus* $\log x$ of $Na_{3-2x}Eu_xP_3O_9N$ shows the slope of −2.0(2), indicating θ = 6 (Fig. S3†). Thus, the electric

dipole–dipole interaction is the main source of non-radiative concentration quenching, producing the low PLQY in this system at high Eu^{2+} concentrations.

Additional differences in the photoluminescent properties of $K_3AlP_3O_9N:Eu^{2+}$ and $Na_3AlP_3O_9N:Eu^{2+}$ are immediately apparent at low temperatures. The emission of the Na^+ analog is blue-shifted and broader (λ_{em} = 429 nm, fwhm = 58 nm, 3217 cm^{-1}) compared to the reported $K_3AlP_3O_9N:Eu^{2+}$ (λ_{em} = 445 nm, fwhm = 54 nm, 2865 cm^{-1}) under 340 nm excitation and at low temperature (77 K). Deconvoluting the spectra into their components indicates that $Na_3AlP_3O_9N:Eu^{2+}$ (Fig. 1b) and $K_3AlP_3O_9N:Eu^{2+}$ (Fig. 1c) can both be fit by three Gaussian peaks with the peak center arising from Eu^{2+} on the [$M^I(1)O_9$] position shifting from 416 nm to 410 nm, Eu^{2+} on the [$M^I(2)O_6N$] position moving from 447 nm to 432 nm, and Eu^{2+} on the [$M^I(3)O_6$] position moving from 465 nm to 462 nm, for the K^+ and Na^+ analogs, respectively. The observed blue shift of each peak is somewhat of a surprise, considering the unit cell volume decreased from 905.5 $Å^3$ to 801.8 $Å^3$ when fully substituting K^+ with Na^+. This would normally suggest an expected redshift of the emission spectrum to the cyan or even green region of the visible spectrum due to stronger CFS. This unexpected blue shift, therefore, must be attributed to weaker CFS stemming from local distortions as the much larger Eu^{2+} is stuffed on the smaller Na^+ site. Such changes are not uncommon. In fact, the most popular example is the blue shift between the commercial yellow-emitting phosphor $Y_3Al_5O_{12}:Ce^{3+}$ and its derivative $Lu_3Al_5O_{12}:Ce^{3+}$. Despite replacing the larger Y^{3+} with the smaller Lu^{3+}, $Lu_3Al_5O_{12}:Ce^{3+}$ shows a blue-shifted green emission because of local distortion coming from the dodecahedral [LuO_8] site than [YO_8] and generates smaller crystal field splitting ($\varepsilon_{cfs,YAG}$ = 3.34 eV, $\varepsilon_{cfs,LuAG}$ = 3.12 eV).[42,43]

Further differences in the optical properties are revealed by monitoring changes in the emission spectrum under various excitation wavelengths (Fig. 2). On the high-energy side of the emission spectrum, the emission from [$Na(1)O_9$] remains unchanged with respect to excitation wavelength, unlike the [$K(1)O_9$] site, which exhibits a significant narrowing of the emission peak. Conversely, longer excitation wavelengths promote longer-wavelength emission from [$Na(3)O_6$], whereas this phenomenon is not observed for [$K(3)O_6$]. The result is that site-selective excitation and preferential thermal quenching fail to narrow the M^I = Na analog. In fact, the emission broadens with excitation, in contrast to the narrower emission obtained for M^I = K with longer excitation wavelengths. The excitation spectra of M^I = Na and M^I = K for λ_{em} = 420 nm and λ_{em} = 450 nm were also measured (Fig. S4†). In both cases, longer wavelength emissions arise from longer wavelength excitations. The shift in excitation of M^I = Na is less than M^I = K, moving from 329 nm for λ_{em} = 420 nm to 340 nm for λ_{em} = 450 nm, while M^I = K moves from 346 nm to 352 nm.

3.2. Fine-tuning the emission spectrum through solid-solutioning: $Na_{2.97}Eu_{0.015}M^{III}P_3O_9N$ (M^{III} = Al, Ga, In)

Substitution on the M^I site clearly results in significant changes to the optical properties. Therefore, the full extent of these changes was further probed by exchanging the M^{III} site. Synthesizing a series of compositional derivatives following $Na_{2.97}Eu_{0.015}M^{III}P_3O_9N$ [M^{III} = Al, ($Al_{0.75}Ga_{0.25}$), ($Al_{0.5}Ga_{0.5}$), ($Al_{0.25}Ga_{0.75}$), Ga, ($Ga_{0.75}In_{0.25}$), ($Ga_{0.5}In_{0.5}$)] was possible under the same synthetic conditions. The purity of polycrystalline products was confirmed by powder X-ray diffraction (Fig. 3a). The peak positions shift to smaller 2θ when Al^{3+} is substituted by Ga^{3+} and Ga^{3+} is substituted by In^{3+}, indicating the larger

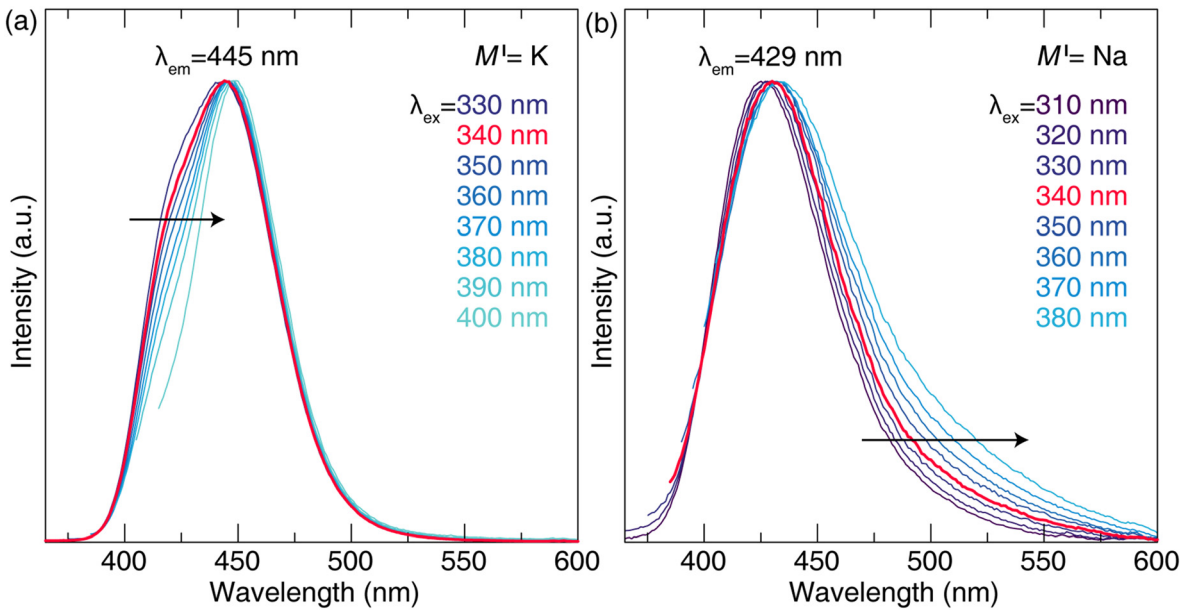

Fig. 2 Emission spectra of (a) $K_3AlP_3O_9N:Eu^{2+}$ and (b) $Na_{2.97}Eu_{0.015}AlP_3O_9N$ under different excitation wavelengths recorded at room temperature show that site-selective excitation on [$Na(1)O_9$] and preferential quenching on [$Na(3)O_6$] do not happen in M^I = Na, unlike M^I = K.

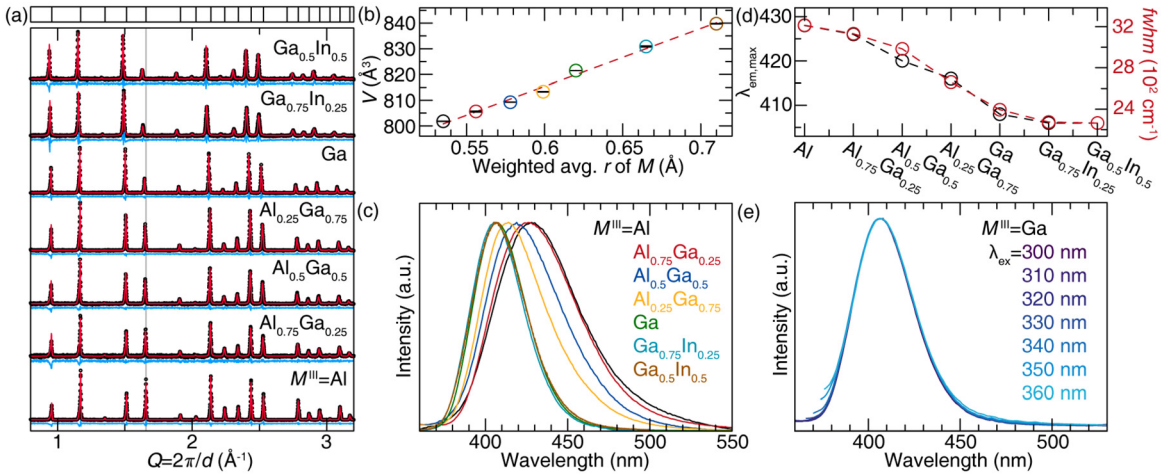

Fig. 3 (a) Le Bail refinements of $Na_{2.97}Eu_{0.015}M^{III}P_3O_9N$ (M^{III} = Al, Ga, In) starting from $Na_3AlP_3O_9N$ structure (ICSD #78373). Peak positions shift towards smaller values in *Q* space along with increments of larger M^{III} elements, Ga^{3+} than Al^{3+} and In^{3+} than Ga^{3+}, which are emphasized by a grey-line around 1.6 $Å^{-1}$. (b) Calculated volumes of the entire series demonstrate a linear increase according to the weighted average radius of M^{III}. (c) Normalized emission spectra of $Na_{2.97}Eu_{0.015}M^{III}P_3O_9N$ under λ_{ex} = 340 nm. (d) The peak positions and fwhm of these emission spectra show that the increment of Ga^{3+} induces more blue-shifted and narrower emissions. However, the substitution of Ga^{3+} by In^{3+} barely influences the emission properties. (e) Emission spectra under different excitations of M^{III} = Ga reveal no significant changes compared to M^{I} = K and M^{I} = Na.

M^{III} ion replaces the smaller ion ($Al^{3+}r_{6\text{-coord}}$ = 0.535 Å, $Ga^{3+}r_{6\text{-coord}}$ = 0.62 Å, $In^{3+}r_{6\text{-coord}}$ = 0.8 Å).[37] All attempts to extend the $Na_{2.97}Eu_{0.015}M^{III}P_3O_9N$ series increasing the In^{3+} content to M^{III} = $Ga_{0.25}In_{0.75}$ and M^{III} = In led to impurities. Indeed, the diffractogram of M^{III} = $Ga_{0.25}In_{0.75}$ (Fig. S5a†) includes unmatched impurity peaks, while analysis by SEM suggests that the product possibly contained indium metal as the ammonia reduced In_2O_3 (Fig. S5b†). In the case of M^{III} = In, the indium metal particles were large enough to be observed by eye.

Le Bail refinements (Table S2†) of the $Na_{2.97}Eu_{0.015}M^{III}P_3O_9N$ series were performed using the $Na_3AlP_3O_9N$ crystal structure file (ICSD #78373) as the starting point. The calculated unit cell volumes of the solid solution series show a linear expansion along the weighted average radius of M^{III}, supporting that Ga^{3+} and In^{3+} replaced Al^{3+} (Fig. 3b). Micrographs collected on an SEM and a subsequent EDS analysis of $Na_{2.97}Eu_{0.015}AlP_3O_9N$ and $Na_{2.97}Eu_{0.015}GaP_3O_9N$ (Fig. S6†) also show that all elements are uniformly distributed in the examined particles and there is no apparent phase or elemental separation. Since the Eu^{2+} concentration (~0.09%) is below the instrument's detection limit, the EDS result for Eu^{2+} is not included in the analysis.

This new $Na_{2.97}Eu_{0.015}M^{III}P_3O_9N$ solid solution shows the counterintuitive relationship between their unitcell volume and photoluminescence properties similar to $M^{I}_{2.97}Eu_{0.015}AlP_3O_9N$. As plotted in Fig. 3c, the solid solution between Al^{3+} and Ga^{3+} (*i.e.*, M^{III} = Al, $Al_{0.75}Ga_{0.25}$, $Al_{0.5}Ga_{0.5}$, $Al_{0.25}Ga_{0.75}$, Ga) reveals blue-shifted emission spectra (M^{III} = Al, λ_{em} = 429 nm; M^{III} = Ga, λ_{em} = 409 nm) with increasing Ga^{3+} (Fig. 3d). This shift seems like following the unit cell expansion of ~2.5% with the incorporation of the larger Ga^{3+}ion, inducing a smaller CFS by enlarging the Eu^{2+} substitution site volume. However, the inclusion of In^{3+} does not lead to an additional shift in the emission spectra despite the unit cell volume expanding another 2.2%. A change in the bandwidth is also observed, with M^{III} = Ga having a narrower fwhm = 42 nm (2493 cm^{-1}) compared to M^{III} = Al having a fwhm = 58 nm (3217 cm^{-1}). The narrower emission when M^{III} = Ga originates from the lack of $[Na(3)O_6]$ site emission, supported by Gaussian fitting. The emission spectra are all identical for each excitation spectrum, unlike M^{III} = Al (Fig. 3e). Exchanging Ga^{3+} for In^{3+} again does not change the peak shape.

Collecting the emission spectra of $Na_{2.97}Eu_{0.015}M^{III}P_3O_9N$ [M^{III} = Al, ($Al_{0.75}Ga_{0.25}$), ($Al_{0.5}Ga_{0.5}$), ($Al_{0.25}Ga_{0.75}$), Ga, ($Ga_{0.75}In_{0.25}$), ($Ga_{0.5}In_{0.5}$)] at low temperature (15 K) and comparing these results to room temperature provides additional insights into the photoluminescent properties. Deconvoluting each emission demonstrates that the photoluminescence of the $M^{I}M^{III}P_3O_9N$ system is independent of the unit cell volume. The M^{III} = Al emission spectrum with Gaussian function at 15 K reveals a good fit with three curves (Fig. 4a). Three peaks are also used to describe the data at 300 K, with the only differences being thermally induced spectral broadening and each peak position slightly blue-shifted, which can be explained by unit-cell thermal expansion (Fig. 4b) and/or contribution from transitions from thermally populated higher-energy vibronic levels of the $5d_1$ emitting level. In M^{III} = $Al_{0.5}Ga_{0.5}$, the emission intensity at 15 K (Fig. 4c) and 300 K (Fig. 4d) increases for Eu^{2+} on the $[Na(1)O_9]$ site whereas the emission from Eu^{2+} on the $[Na(2)O_6N]$ and $[Na(3)O_6]$ sites diminishes. When Al^{3+} is fully exchanged for Ga^{3+}, the emission from Eu^{2+} on the $[Na(1)O_9]$ increases further, Eu^{2+} on the

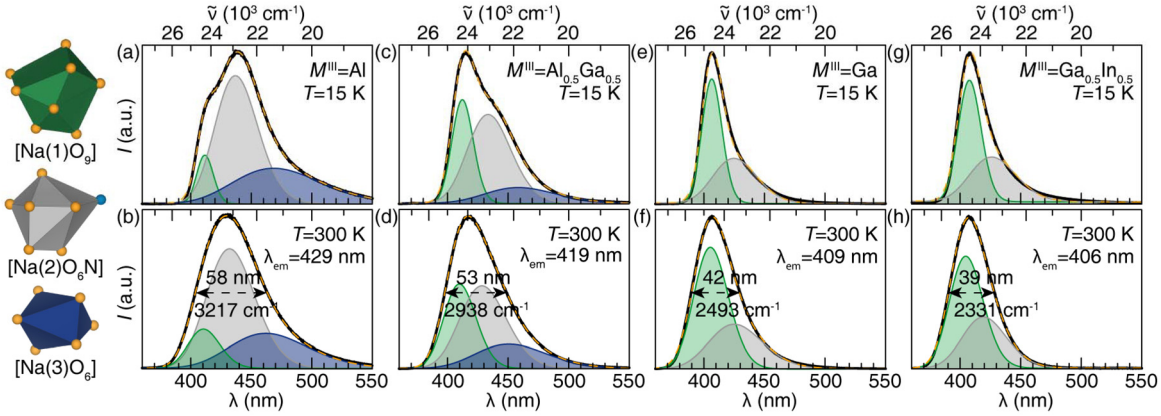

Fig. 4 In the $Na_{2.97}Eu_{0.015}M^{III}P_3O_9N$ series, emission spectra are measured under 340 nm excitation at T = 15 K and T = 300 K. Emission spectra of M^{III} = Al (a) at T = 15 K, (b) at T = 300 K, and M^{III} = $Al_{0.5}Ga_{0.5}$ (c) at T = 15 K, (d) at T = 300 K are deconvoluted in three peaks from each Na^+ sites. With the absence of Al^{3+}, the peak from [Na(3)O_6] is quenched in M^{III} = Ga (e) at T = 15 K, (f) at T = 300 K, and M^{III} = $Ga_{0.5}In_{0.5}$ (g) at T = 15 K, (h) at T = 300 K.

[Na(2)O_6N] shows a greater decrease, and the emission from Eu^{2+} on the [Na(3)O_6] is entirely lost even at low temperature. Meanwhile, the peak positions of Eu^{2+} on [Na(1)O_9] and Eu^{2+} on [Na(2)O_6N] are mostly preserved at around 410 nm and 430 nm, respectively. As a result of the strong preference for Eu^{2+} to occupy the [Na(1)O_9] site, the total emission spectrum is noticeably blue-shifted and narrowed. It can be explained by the possibility that Ga^{3+} induces more distortion on the smallest 6-coordinated cation site, making it too small to be substituted by Eu^{2+} or the nearest neighbor impact. Interestingly, incrementing In^{3+} into Ga^{3+} generates no remarkable differences in the emission spectrum (Fig. 4g). The emission of M^{III} = $Ga_{0.5}In_{0.5}$ at T = 300 K also shows a narrowed spectrum with a slightly shifted [Na(2)O_6N] emission peak.

3.3. Thermal and chromatic stability changes in $Na_{2.97}Eu_{0.015}M^{III}P_3O_9N$

The operating temperature of a commercial LED package is approximately 423 K.[7] Thus, the emission intensity should be thermally robust against any thermal quenching processes at such a temperature. This is often qualitatively analyzed by the thermal quenching temperature (T_{50}), in which the relative emission intensity drops by 50%. Temperature-dependent emission measurements were conducted to study the series' thermal stability (Fig. 5a–d). At M^{III} = Al, the T_{50} shows an extrapolated value of 610 K, which is relatively high compared to other reported commercial thermally stable phosphors (YAG:Ce^{3+}, T_{50} ≈ 632K; BAM:Eu^{2+}, T_{50} ≈ 650K).[44,45] Although

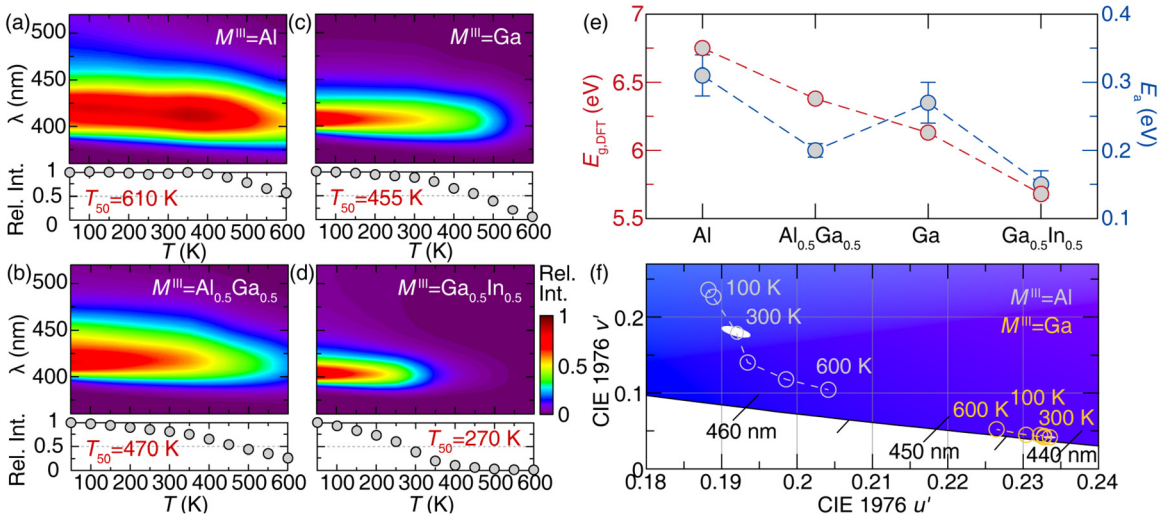

Fig. 5 Temperature-dependent emission of $Na_{2.97}Eu_{0.015}M^{III}P_3O_9N$ series at (a) M^{III} = Al, (b) M^{III} = $Al_{0.5}Ga_{0.5}$, (c) M^{III} = Ga, and (d) M^{III} = $Ga_{0.5}In_{0.5}$. T_{50} decreases along the diminishing host structure's bandgap. (e) Calculated E_g using diffuse reflectance spectrum and E_a values using temperature-dependent emission spectra of $Na_{2.97}Eu_{0.015}M^{III}P_3O_9N$ series (f) Changes in chromaticity by increasing temperature in CIE 1976 space of M^{III} = Al and M^{III} = Ga plotted with 3-step MacAdam ellipse at 300 K.

the T_{50} decreases with an incremental Ga^{3+} to 470 K for M^{III} = $Al_{0.5}Ga_{0.5}$ and to 455 K for M^{III} = Ga, their values are still reasonably thermally stable, showing higher values than 423 K. Here, In^{3+} dramatically reduces the photoluminescence thermal stability, decreasing the T_{50} for M^{III} = $Ga_{0.5}In_{0.5}$ to 270 K with almost zero intensity at 423 K. To explain the reduced thermal stability, changes in the bandgap of hosts along their composition alteration should be examined first. The bandgap of $Na_3M^{III}P_3O_9N$ was calculated by DFT. Theoretically, M^{III} = Al should have the highest E_g because of aluminum's smaller electronegativity (EN) than Ga^{3+} or In^{3+} (χ_{Al} = 1.61, χ_{Ga} = 1.81, χ_{In} = 1.78), which makes a more considerable EN difference between phosphorus, oxygen, and nitrogen. The calculated $E_{g,DFT}$ values are 6.75 eV for M^{III} = Al, 6.38 eV for M^{III} = $Al_{0.5}Ga_{0.5}$, 6.21 eV for M^{III} = Ga, and 5.70 eV for M^{III} = $Ga_{0.5}In_{0.5}$ (Fig. 5e). Based on the bandgap values, the decreasing T_{50} can be explained by the thermally activated photoionization, which occurs more readily with a smaller bandgap.[46]

Although the E_g values nicely explain the thermal stability for M^{III} = Al, $Al_{0.5}Ga_{0.5}$, and Ga, further explanation is required for the low thermal stability of M^{III} = $Ga_{0.5}In_{0.5}$. The position of the Eu^{2+} 5d orbital energy levels is splitting due to CFS, and once the electron on the most stabilized $5d_1$ level is excited by the thermal energy, it can be transferred into the host's conduction band, creating non-radiative relaxation and diminishing the photoluminescence intensity.[47,48] The smaller bandgap decreases the energy level of the conduction band, enhancing photoionization quenching. The activated energy (E_a), which is the energy gap between the edge of the conduction band and the $5d_1$ level of Eu^{2+}, determines the degree of the quenching process. From the temperature-dependent emission spectra, the E_a values can be estimated by the Arrhenius dependence, as depicted by eqn (4),

$$I(T) = \frac{I_0}{1 + Ae^{(-E_a/kT)}} \quad (4)$$

where I_0 is the initial intensity, E_a is the activation energy, k is the Boltzmann constant, and T is the temperature. For M^{III} = Al, E_a is 0.31(3) eV, while M^{III} = $Al_{0.5}Ga_{0.5}$ and M^{III} = Ga gives lower values of 0.20(1) eV and 0.27(3) eV (Fig. S7†). The E_a of M^{III} = $Ga_{0.5}In_{0.5}$ shows the lowest value of 0.15(2) eV, corresponding well with the thermal quenching tendency in the series. These estimated E_a values support the lower thermal stability of the In^{3+} containing hosts since thermal ionization can occur more easily with smaller E_a.

Chromatic stability with the increasing temperature is also crucial in the actual application, as is the thermal stability. Since M^{III} = Ga shows less shift in peak position along the temperature due to the lack of $[Na(3)O_6]$ emission, as shown in Fig. 4e, the chromatic stabilities of $Na_{2.97}Eu_{0.015}AlP_3O_9N$ and $Na_{2.97}Eu_{0.015}GaP_3O_9N$ are calculated based on the temperature-dependent emission at each temperature. Coordinates of six different temperatures in the 100–600 K are plotted in CIE 1976 $u'v'$ space with a 3-step MacAdam ellipse, which is presented as a white oval centered at each phosphor's 300 K color coordinate (Fig. 5f). Compared to M^{III} = Al, the shift in emission color of M^{III} = Ga is noticeably smaller for all the temperature ranges. To quantify the color changes, the concept of $\Delta u'\Delta v'$, the distance between the color coordinates at 300 K ($u'_{init.}$, $v'_{init.}$) and the average color coordinate at six different temperatures ($u'_{avg.}$, $v'_{avg.}$), is calculated by following eqn (5).[49]

$$\Delta u'\Delta v' = \sqrt{\left(u'_{avg.} - u'_{init.}\right)^2 + \left(v'_{avg.} - v'_{init.}\right)^2} \quad (5)$$

$Na_{2.97}Eu_{0.015}AlP_3O_9N$ has the higher value of $\Delta u'\Delta v'$ = 0.0119 than $Na_{2.97}Eu_{0.015}GaP_3O_9N$ whose value is $\Delta u'\Delta v'$ = 0.0038, supporting M^{III} = Ga is more chromatically stable.

3.4. Quantum yield analysis through thermoluminescence of $Na_{2.97}Eu_{0.015}M^{III}P_3O_9N$

Even though the phosphor's thermal stability is satisfactory, the photoluminescent quantum yield should be higher for application. The most common commercial blue, BAM:Eu^{2+}, and green, β-SiAlON:Eu^{2+}, phosphors often show a PLQY > 90%. The PLQY of the $Na_{2.97}Eu_{0.015}M^{III}P_3O_9N$ solid solution was measured to investigate how the cation substitution in the host affects PLQY. Interestingly, PLQY increases from 21(2)% to 54(2)% between Al^{3+} to Ga^{3+} compositions, inversely related to the E_g and E_a tendencies (Fig. 6a). However, the introduction of In^{3+} rapidly quenches the PLQY to 2.2(4)%, indicating that the low quantum yield is related to the small E_a and room-temperature thermal photoionization. The trend in quantum yield as a function of M^{III} cation was also investigated in greater depth.

Due to the aliovalent substitution between Na^+ and Eu^{2+}, the inherent defect should occur to compensate for the charge valence. The most probable charge-neutral defect configurations are depicted in Kröger–Vink notation,

$$Na^{\times}_{Na} + Na^{\times}_{Na} \rightarrow Eu^{\cdot}_{Na} + V'_{Na} \quad (6)$$

$$Na^{\times}_{Na} + O^{\times}_{O} \rightarrow Eu^{\cdot}_{Na} + N'_{O} \quad (7)$$

where V refers to a vacancy site, subscript refers to the cation site, and superscript means the cation position, ×, ˙, and ′ refer to neutral, positive, and negative charge, respectively.[50] Other common types of defects, like point defects and antisite defects, also can impact the $Na_{2.97}Eu_{0.015}M^{III}P_3O_9N$ series photoluminescence. To understand how the influence of defects along the cation substitution on M^{III} differs in the host system, TL glow curves are analyzed (Fig. 6b–e). The intensity of each TL curve was divided by a thermal quenching profile to correct the temperature dependency (TD) before being analyzed. Since the emission of M^{III} = $Ga_{0.5}In_{0.5}$ is mostly quenched after 400 K, the noise in its TL curve after 500 K is exaggerated by the TD correction; thus, the fitting was done before 500 K.

The peak positions and dosimetry parameters of trap states are determined using the glow curve deconvolution method. Deconvolution of each TL glow curve is performed with the

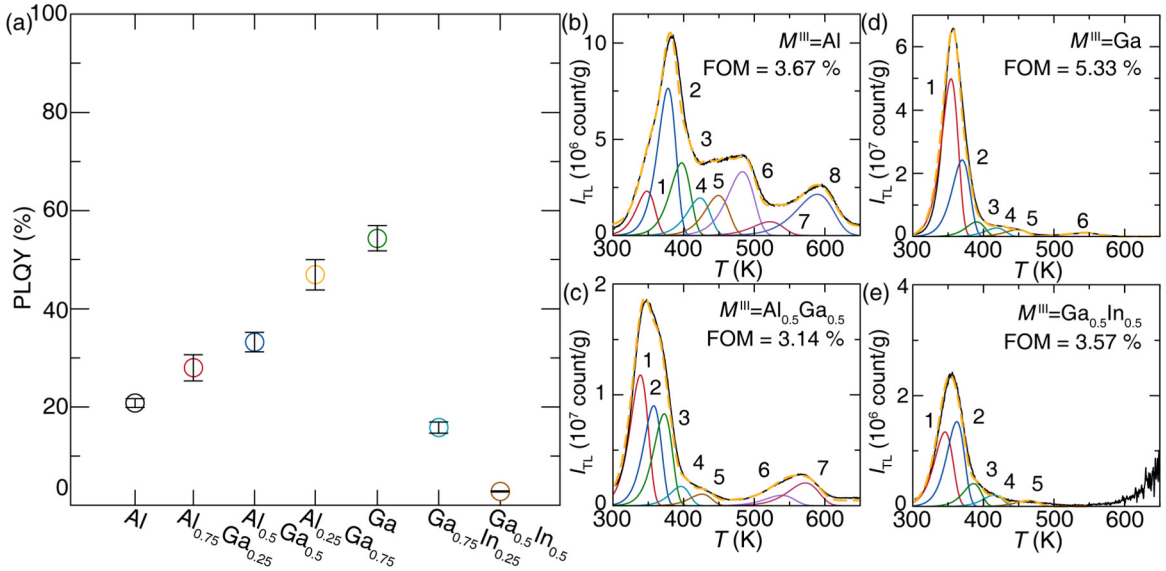

Fig. 6 (a) Room-temperature PLQY of $Na_{2.97}Eu_{0.015}M^{III}P_3O_9N$. M^{III} = Ga shows the highest value, which is almost three times as large as M^{III} = Al. The increment In^{3+} significantly drops PLQY. TL glow curves of the solid solution at (b) M^{III} = Al, (c) M^{III} = $Al_{0.5}Ga_{0.5}$, (d) M^{III} = Ga, and (e) M^{III} = $Ga_{0.5}In_{0.5}$. Each curve is deconvoluted with the Randall–Wilkins equation.

GlowFit2 software using an approximation of the first-order kinetics Randall–Wilkins equation (eqn (8)).[51,52]

$$I = n_0 s \exp\left(-\frac{E}{kT}\right) \exp\left(-\int_0^T \frac{s \exp\left(-\frac{E}{kT}\right)}{\beta} \mathrm{d}T\right) \quad (8)$$

where I is the TL intensity, n_0 is the number of trapped electrons, s is the frequency factor, E is trap depth, k is Planck constant, T is temperature, and β is the heating rate. The area of each curve represents the bound electron population. The deconvolution parameters of each TL curve are plotted in Table 1. The values of E and s can evaluate the reliability of fitting. Additionally, since the s reflects the interaction between the trap-bounded electron and the lattice phonon, the maximum value of s should be the same or lower than the lattice vibration of the host. In the $Na_3M^{III}P_3O_9N$ (M^{III} = Al, Ga, In), the vibrations of O–N, O–P, N–P, and M^{III}–O are generally between 1000–1100 cm^{-1}, 900–1000 cm^{-1}, 1100–1200 cm^{-1}, and 400–650 cm^{-1}, respectively, which correspond to the range from 1.2×10^{13} to 3.6×10^{13} s^{-1}.[53–56] The s values extracted from the fitting are primarily between 1×10^{11} and 3×10^{12}, supporting the validity of TL deconvolution.

Table 1 Parameters of calculated trap states using thermoluminescence glow curves

(a) $Na_{2.97}Eu_{0.015}AlP_3O_9N$

Trap no.	T (K)	E (eV)	s (s^{-1})
1	349.00	0.79	1.73×10^{11}
2	378.81	0.92	3.39×10^{12}
3	397.98	0.94	3.54×10^{11}
4	424.00	0.95	1.03×10^{11}
5	450.00	1.01	1.35×10^{11}
6	483.90	1.04	4.86×10^{10}
7	522.60	1.05	6.43×10^{9}
8	589.50	1.12	1.26×10^{9}

(b) $Na_{2.97}Eu_{0.015}Al_{0.5}Ga_{0.5}P_3O_9N$

Trap no.	T (K)	E (eV)	s (s^{-1})
1	338.83	0.77	1.86×10^{11}
2	357.71	0.87	1.47×10^{12}
3	372.56	0.90	1.24×10^{12}
4	396.30	0.97	1.54×10^{12}
5	426.01	0.99	3.38×10^{11}
6	538.80	1.19	6.05×10^{10}
7	572.50	1.29	9.43×10^{10}

(c) $Na_{2.97}Eu_{0.015}GaP_3O_9N$

Trap no.	T (K)	E (eV)	s (s^{-1})
1	354.12	0.90	6.19×10^{12}
2	370.02	0.91	2.17×10^{12}
3	390.48	0.98	3.09×10^{12}
4	418.69	1.03	1.50×10^{12}
5	448.24	1.07	5.80×10^{11}
6	542.69	1.15	1.97×10^{10}

(d) $Na_{2.97}Eu_{0.015}Ga_{0.5}In_{0.5}P_3O_9N$

Trap no.	T (K)	E (eV)	s (s^{-1})
1	345.61	0.77	1.47×10^{11}
2	362.30	0.90	2.45×10^{12}
3	385.96	0.99	7.34×10^{12}
4	415.19	1.04	2.83×10^{12}
5	464.21	1.13	1.22×10^{12}

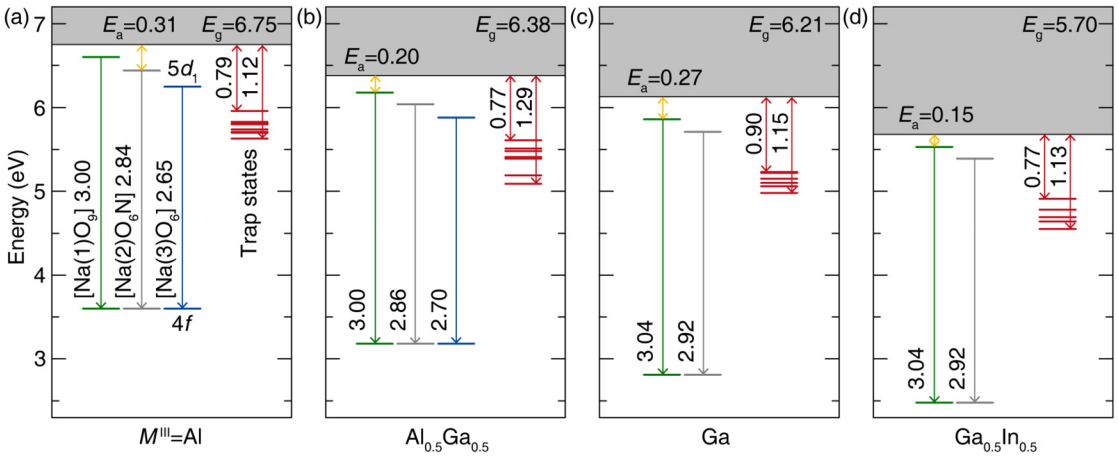

Fig. 7 Emission mechanism diagrams for (a) M^{III} = Al, (b) M^{III} = $Al_{0.5}Ga_{0.5}$, (c) M^{III} = Ga, and (d) M^{III} = $Ga_{0.5}In_{0.5}$.

Notably, M^{III} = Al exhibits eight pronounced peaks (Fig. 6b), and at least those numbered 3–8 are deep enough to immobilize the excited carriers for basically infinite time under ambient conditions. This phenomenon elucidates the low quantum yield observed in M^{III} = Al, as a significant portion of the excited electron population becomes trapped in various states, inhibiting photoluminescence despite the host material possessing the largest band gap and activation energy within the solid solution series. Along with the increasing Ga^{3+}, the number of trap states and the portion of higher energy trap states decrease noticeably, supporting the highest PLQY at M^{III} = Ga, for which no significant TL appears above 400 K. Incrementally increasing In^{3+} does not show noticeable changes in trap states, indicating its low PLQY mainly stems from thermal quenching rather than defect quench. These results enable the construction of a luminescence mechanism for each composition. Combining the electronic structure (calculated E_g), photoluminescence, and thermoluminescence for the $Na_{2.97}Eu_{0.015}M^{III}P_3O_9N$ in Fig. 7 demonstrates that the balance of band gap, trap depths, and 4f↔5d transition give M^{III} = Ga the best overall optical properties with the narrowest emission.

4. Conclusion

This series of Eu^{2+}-substituted $Na_3M^{III}P_3O_9N$ (M^{III} = Al, $Al_{0.75}Ga_{0.25}$, $Al_{0.5}Ga_{0.5}$, $Al_{0.25}Ga_{0.75}$, Ga, $Ga_{0.75}In_{0.25}$, $Ga_{0.5}In_{0.5}$) phosphors was successfully synthesized using gas reduction nitridation. Powder X-ray diffraction confirmed the quality of the products from the synthesis while photoluminescence measurement at low temperature supports that Eu^{2+} replaces three crystallographically independent Na^+ sites in $Na_{2.97}Eu_{0.015}AlP_3O_9N$. Interestingly, incorporating Ga^{3+} shifts the site selectivity so Eu^{2+} prefers only two substitution sites, [Na(1)O$_9$] and [Na(2)O$_6$N]. $Na_{2.97}Eu_{0.015}AlP_3O_9N$ generates 429 nm violet emission with fwhm = 58 nm (3217 cm^{-1}). As Ga^{3+} increases, it appears there must be a distortion in the crystal structure, generating more blue-shifted emission further compounded by the lack of Eu^{2+} on the [Na(3)O$_6$] crystallographic site. This allows narrower emission with fwhm = 42 nm (2493 cm^{-1}) in $Na_{2.97}Eu_{0.015}GaP_3O_9N$ with λ_{em} = 409 nm. The presence of Ga^{3+} also provides a decent T_{50} = 455 K, while $Na_{2.97}Eu_{0.015}GaP_3O_9N$ shows high chromatic stability. Additionally, PLQY of $Na_{2.97}Eu_{0.015}GaP_3O_9N$ is the highest among the series, with a reasonable value of 54(2) %, worthy of further optimization efforts. Thermoluminescence analysis supports that the highest quantum yield of M^{III} = Ga originates from a smaller number of deep trap states that minimize their deleterious impact on excited electrons. This study of the $Na_{2.97}Eu_{0.015}M^{III}P_3O_9N$ series offers that cation substitution on the host can accompany the preferred cation site selectivity, generating narrow and thermally and chromatically stable emission. This may be taken as proof that deliberately executed cation substitution may be an efficient approach for modeling and tuning important phosphors' properties, among them for designing narrow-emitting and chromatically stable phosphors.

Author contributions

Nakyung Lee: conceptualization, data curation, formal analysis, investigation, visualization, writing – original draft. Justyna Zeler: data curation, formal analysis, funding acquisition, investigation, writing – review & editing. Małgorzata Sójka: conceptualization, writing – review & editing. Eugeniusz Zych: resources, writing – review & editing. Jakoah Brgoch: conceptualization, funding acquisition, project administration, supervision, writing – review & editing.

Data availability

The data supporting this article have been included as part of the ESI.†

Conflicts of interest

The authors declare no competing financial interest.

Acknowledgements

The National Science Foundation (DMR-2349319) and the Welch Foundation (E-2181) for supporting this work. J. Z. acknowledges support from the National Science Center (NCN) Poland project 2023/49/B/ST5/04265.

References

1 P. Pust, P. J. Schmidt and W. Schnick, A Revolution in Lighting, *Nat. Mater.*, 2015, **14**(5), 454–458, DOI: 10.1038/nmat4270.
2 N. C. George, K. A. Denault and R. Seshadri, Phosphors for Solid-State White Lighting, *Annu. Rev. Mater. Res.*, 2013, **43**, 481–501, DOI: 10.1146/annurev-matsci-073012-125702.
3 A. G. Bispo-Jr, L. F. Saraiva, S. A. M. Lima, A. M. Pires and M. R. Davolos, Recent Prospects on Phosphor-Converted LEDs for Lighting, Displays, Phototherapy, and Indoor Farming, *J. Lumin.*, 2021, **237**, 118167, DOI: 10.1016/j.jlumin.2021.118167.
4 R. Gautier, X. Li, Z. Xia and F. Massuyeau, Two-Step Design of a Single-Doped White Phosphor with High Color Rendering, *J. Am. Chem. Soc.*, 2017, **139**(4), 1436–1439, DOI: 10.1021/jacs.6b12597.
5 Z. T. Kazanasmaz, F. B. Köse and G. Tayfur, Emerging Concept of Human Centric Lighting in Literature Review, EEEIC/I&CPS Europe, 2023, pp. 1–6. DOI:DOI: 10.1109/EEEIC/ICPSEurope57605.2023.10194800.
6 W. Tang, J. G. Liu and C. Shen, Blue Light Hazard Optimization for High Quality White LEDs, *IEEE Photonics J.*, 2018, **10**(5), 1–10, DOI: 10.1109/JPHOT.2018.2867822.
7 Department of Energy, 2022 Solid-State Lighting R&D Opportunities, https://www.energy.gov/eere/ssl/articles/doe-publishes-2022-solid-state-lighting-rd-opportunities.
8 S. Li, R.-J. Xie, T. Takeda and N. Hirosaki, Critical Review—Narrow-Band Nitride Phosphors for Wide Color-Gamut White LED Backlighting, *ECS J. Solid State Sci. Technol.*, 2018, **7**(1), R3064, DOI: 10.1149/2.0051801jss.
9 M. Zhao, H. Liao, L. Ning, Q. Zhang, Q. Liu and Z. Xia, Next-Generation Narrow-Band Green-Emitting RbLi$(Li_3SiO_4)_2$:Eu^{2+} Phosphor for Backlight Display Application, *Adv. Mater.*, 2018, **30**(38), 1802489, DOI: 10.1002/adma.201802489.
10 E. H. Song, Y. Y. Zhou, Y. Wei, X. X. Han, Z. R. Tao, R. L. Qiu, Z. G. Xia and Q. Y. Zhang, A Thermally Stable Narrow-Band Green-Emitting Phosphor $MgAl_2O_4$:Mn^{2+} for Wide Color Gamut Backlight Display Application, *J. Mater. Chem. C*, 2019, **7**(27), 8192–8198, DOI: 10.1039/C9TC02107H.
11 S. Hariyani, M. Sójka, A. Setlur and J. Brgoch, A Guide to Comprehensive Phosphor Discovery for Solid-State Lighting, *Nat. Rev. Mater.*, 2023, **8**(11), 759–775, DOI: 10.1038/s41578-023-00605-6.
12 D. L. MacAdam, Visual Sensitivities to Color Differences in Daylight, *J. Opt. Soc. Am.*, 1942, **32**(5), 247–274, DOI: 10.1364/JOSA.32.000247.
13 T. Takeda, R.-J. Xie, T. Suehiro and N. Hirosaki, Nitride and Oxynitride Phosphors for White LEDs: Synthesis, New Phosphor Discovery, Crystal Structure, *Prog. Solid State Chem.*, 2018, **51**, 41–51, DOI: 10.1016/j.progsolidstchem.2017.11.002.
14 H. Terraschke and C. Wickleder, UV, Blue, Green, Yellow, Red, and Small: Newest Developments on Eu^{2+}-Doped Nanophosphors, *Chem. Rev.*, 2015, **115**(20), 11352–11378, DOI: 10.1021/acs.chemrev.5b00223.
15 C. K. Jørgensen, Fractional Charges, Integral Oxidation States and the Nephelauxetic Effect in the Five Transition Groups, *Helv. Chim. Acta*, 1967, **50**(S1), 131–146, DOI: 10.1002/hlca.19670500911.
16 P. Dorenbos, The Nephelauxetic Effect on the Electron Binding Energy in the 4*f* Ground State of Lanthanides in Compounds, *J. Lumin.*, 2019, **214**, 116536, DOI: 10.1016/j.jlumin.2019.116536.
17 A. L. Tchougréeff and R. Dronskowski, Nephelauxetic Effect Revisited, *Int. J. Quantum Chem.*, 2009, **109**(11), 2606–2621, DOI: 10.1002/qua.21989.
18 P. Dorenbos, 5*d*-level energies of and the crystalline environment. III. Oxides containing ionic complexes, *Phys. Rev. B: Condens. Matter Mater. Phys.*, 2001, **64**, 125117 https://journals.aps.org/prb/abstract/10.1103/PhysRevB.64.125117.
19 P. Dorenbos, Crystal Field Splitting of Lanthanide $4f^{n-1}5d$-Levels in Inorganic Compounds, *J. Alloys Compd.*, 2002, **341**(1), 156–159, DOI: 10.1016/S0925-8388(02)00056-7.
20 S. Wendl, M. Mallmann, P. Strobel, P. J. Schmidt and W. Schnick, Ammonothermal Synthesis of Ba_2PO_3N – An Oxonitridophosphate with Non-Condensed PO_3N Tetrahedra, *Eur. J. Inorg. Chem.*, 2020, **2020**(10), 841–846, DOI: 10.1002/ejic.202000041.
21 M. Derbel and A. Mbarek, Solid State Synthesis and Luminescent Properties of Bright Blue-Emitting $Ba_2P_2O_7$:Eu^{2+} Phosphor, *SN Appl. Sci.*, 2020, **2**(4), 562, DOI: 10.1007/s42452-020-2329-8.
22 Z. Xia, M. S. Molokeev, W. B. Im, S. Unithrattil and Q. Liu, Crystal Structure and Photoluminescence Evolution of $La_5(Si_{2+x}B_{1-x})(O_{13-x}N_x)$:$Ce^{3+}$ Solid Solution Phosphors, *J. Phys. Chem. C*, 2015, **119**(17), 9488–9495, DOI: 10.1021/acs.jpcc.5b01211.
23 H. Ji, Z. Huang, Z. Xia, M. S. Molokeev, V. V. Atuchin, M. Fang and Y. Liu, Discovery of New Solid Solution Phosphors via Cation Substitution-Dependent Phase Transition in $M_3(PO_4)_2$:Eu^{2+} (M = Ca/Sr/Ba) Quasi-Binary Sets, *J. Phys. Chem. C*, 2015, **119**(4), 2038–2045, DOI: 10.1021/jp509743r.
24 K. Zhao, L. Yin, Z. Ma, T. Yang, H. Tang, P. Cao and S. Huang, Investigation of the Solid-Solution Limit, Crystal

Structure, and Thermal Quenching Mitigation of Sr-Substituted $Rb_2CaP_2O_7$:Eu^{2+} Phosphors for White LED Applications, *Inorg. Chem.*, 2022, **61**(3), 1627–1635, DOI: 10.1021/acs.inorgchem.1c03470.

25 A. P. Black, K. A. Denault, C. Frontera, R. Seshadri, A. R. Goñi and A. Fuertes, Emission Colour Tuning through Coupled N/La Introduction in Sr_2SiO_4:Eu^{2+}, *J. Mater. Chem. C*, 2015, **3**(43), 11471–11477, DOI: 10.1039/C5TC02437D.

26 D. Wu, C. Shi, J. Zhou, Y. Gao, Y. Huang, J. Ding and Q. Wu, Full-Visible-Spectrum Lighting Enabled by Site-Selective Occupation in the High Efficient and Thermal Stable $(Rb,K)_2CaPO_4F$: Eu^{2+} Solid-Solution Phosphors, *Chem. Eng. J.*, 2022, **430**, 133062, DOI: 10.1016/j.cej.2021.133062.

27 S. Hariyani, X. Xing, M. Amachraa, J. Bao, S. P. Ong and J. Brgoch, Realizing Wide-Gamut Human-Centric Display Lighting with $K_3AlP_3O_9N$:Eu^{2+}, *Adv. Opt. Mater.*, 2023, **11**(8), 2202689, DOI: 10.1002/adom.202202689.

28 B. H. Toby and R. B. Von Dreele, GSAS-II: The Genesis of a Modern Open-Source All Purpose Crystallography Software Package, *J. Appl. Crystallogr.*, 2013, **46**(2), 544–549, DOI: 10.1107/S0021889813003531.

29 P. E. Blöchl, Projector Augmented-Wave Method, *Phys. Rev. B:Condens. Matter Mater. Phys.*, 1994, **50**(24), 17953–17979, DOI: 10.1103/PhysRevB.50.17953.

30 G. Kresse and J. Furthmüller, Efficient Iterative Schemes for Ab Initio Total-Energy Calculations Using a Plane-Wave Basis Set, *Phys. Rev. B:Condens. Matter Mater. Phys.*, 1996, **54**(16), 11169–11186, DOI: 10.1103/PhysRevB.54.11169.

31 J. P. Perdew, K. Burke and M. Ernzerhof, Generalized Gradient Approximation Made Simple, *Phys. Rev. Lett.*, 1996, **77**(18), 3865–3868, DOI: 10.1103/PhysRevLett.77.3865.

32 W. Sun, S. Dacek, S. Ong, G. Hautier, A. Jain, W. Richards, A. Gamst and K. Persson, The thermodynamic scale of inorganic crystalline metastability, *Sci. Adv.*, 2016, **2**, e1600225, DOI: 10.1126/sciadv.1600225.

33 J. Heyd, G. E. Scuseria and M. Ernzerhof, Erratum: "Hybrid Functionals Based on a Screened Coulomb Potential", [J. Chem. Phys. 118, 8207(2003)], *J. Chem. Phys.*, 2006, **21**(124), 219906, DOI: 10.1063/1.2204597.

34 J. C. de Mello, H. F. Wittmann and R. H. Friend, An Improved Experimental Determination of External Photoluminescence Quantum Efficiency, *Adv. Mater.*, 1997, **9**(3), 230–232, DOI: 10.1002/adma.19970090308.

35 J. Mooney and P. Kambhampati, Get the Basics Right: Jacobian Conversion of Wavelength and Energy Scales for Quantitative Analysis of Emission Spectra, *J. Phys. Chem. Lett.*, 2013, **4**(19), 3316–3318, DOI: 10.1021/jz401508t.

36 W. Feldmann, Über Nitridophosphate $MI3M^{III}P_3O_9N$ (M^{I} = Na; K, M^{III} = Al; Ga; Cr; Fe; Mn), *Z. Chem.*, 1987, **27**(5), 182–183, DOI: 10.1002/zfch.19870270515.

37 R. D. Shannon, Revised Effective Ionic Radii and Systematic Studies of Interatomic Distances in Halides and Chalcogenides, *Acta Crystallogr., Sect. A*, 1976, **32**(5), 751–767, DOI: 10.1107/S0567739476001551.

38 W. Feldmann, Über Natrium-Aluminium-Nitridophosphat $Na_3AlP_3O_9N$ Und Natrium-Magnesium-Nitridophosphat $Na_2Mg_2P_3O_9N$, *Z. Chem.*, 1987, **27**(3), 100–101, DOI: 10.1002/zfch.19870270309.

39 D. Massiot, R. Conanec, W. Feldmann, R. Marchand and Y. Laurent, NMR Characterization of the $Na_3AlP_3O_9N$ and $Na_2Mg_2P_3O_9N$ Nitridophosphates: Location of the (NaAl)/Mg_2 Substitution, *Inorg. Chem.*, 1996, **35**(17), 4957–4960, DOI: 10.1021/ic960164+.

40 G. Blasse, Energy Transfer in Oxidic Phosphors, *Phys. Lett. A*, 1968, **28**(6), 444–445, DOI: 10.1016/0375-9601(68)90486-6.

41 L. G. V. Uitert, Characterization of Energy Transfer Interactions between Rare Earth Ions, *J. Electrochem. Soc.*, 1967, **114**(10), 1048, DOI: 10.1149/1.2424184.

42 S. Hu, M. Ju, P. Wang, M. Zhong, C. Zhang and Y. Jin, Investigation of the Microstructure and Electronic Features for Ce^{3+}-Doped YAG Crystal: A First-Principle Study, *Comput. Mater. Sci.*, 2021, **200**, 110762, DOI: 10.1016/j.commatsci.2021.110762.

43 C. F. Varela, Y. D. Molina, S. S. Gutiérrez, L. C. Moreno-Aldana and C. A. P. Vargas, Optical and Structural Properties of the Fe^{3+}-Doped $Lu_3Al_5O_{12}$:Ce^{3+} Garnet Phosphor, *RSC Adv.*, 2021, **11**(20), 11804–11812, DOI: 10.1039/D1RA01345A.

44 Y.-C. Lin, M. Bettinelli, S. K. Sharma, B. Redlich, A. Speghini and M. Karlsson, Unraveling the Impact of Different Thermal Quenching Routes on the Luminescence Efficiency of the $Y_3Al_5O_{12}$:Ce^{3+} Phosphor for White Light Emitting Diodes, *J. Mater. Chem. C*, 2020, **8**(40), 14015–14027, DOI: 10.1039/D0TC03821K.

45 H. Zhu, H. Yang, W. Fu, P. Zhu, M. Li, Y. Li, Y. Sui, S. Liu and G. Zou, The Improvement of Thermal Stability of $BaMgAl_{10}O_{17}$:Eu^{2+} Coated with MgO, *Mater. Lett.*, 2008, **62**(4), 784–786, DOI: 10.1016/j.matlet.2007.06.060.

46 J. Ueda, P. Dorenbos, A. J. J. Bos, A. Meijerink and S. Tanabe, Insight into the Thermal Quenching Mechanism for $Y_3Al_5O_{12}$:Ce^{3+} through Thermoluminescence Excitation Spectroscopy, *J. Phys. Chem. C*, 2015, **119**(44), 25003–25008, DOI: 10.1021/acs.jpcc.5b08828.

47 Y. Wei, L. Cao, L. Lv, G. Li, J. Hao, J. Gao, C. Su, C. C. Lin, H. S. Jang, P. Dang and J. Lin, Highly Efficient Blue Emission and Superior Thermal Stability of $BaAl_{12}O_{19}$:Eu^{2+} Phosphors Based on Highly Symmetric Crystal Structure, *Chem. Mater.*, 2018, **30**(7), 2389–2399, DOI: 10.1021/acs.chemmater.8b00464.

48 J. Ueda, P. Dorenbos, A. J. J. Bos, A. Meijerink and S. Tanabe, Insight into the Thermal Quenching Mechanism for $Y_3Al_5O_{12}$:Ce^{3+} through Thermoluminescence Excitation Spectroscopy, *J. Phys. Chem. C*, 2015, **119**(44), 25003–25008, DOI: 10.1021/acs.jpcc.5b08828.

49 M. Sójka, S. Hariyani, N. Lee and J. Brgoch, Colossal Chromatic Shift in the $Ba_2Ca_2B_4O_{10}$:Ce^{3+}Phosphor, *Chem. Mater.*, 2023, **35**, 6491–6501 https://pubs.acs.org/doi/10.1021/acs.chemmater.3c01465.

50 F. A. Kröger and H. J. Vink, Relations between the Concentrations of Imperfections in Crystalline Solids, in *Solid State Physics*, Academic Press, 1956, vol. 3, pp. 307–435. DOI: 10.1016/S0081-1947(08)60135-6.

51 J. T. Randall, M. H. F. Wilkins and M. L. E. Oliphant, Phosphorescence and Electron Traps - I. The Study of Trap Distributions, *Proc. R. Soc. London, Ser. A*, 1997, **184**(999), 365–389, DOI: **10.1098/rspa.1945.0024**.

52 M. Puchalska and P. Bilski, GlowFit—a New Tool for Thermoluminescence Glow-Curve Deconvolution, *Radiat. Meas.*, 2006, **41**(6), 659–664, DOI: **10.1016/j.radmeas.2006.03.008**.

53 J. J. Benítez, A. Díaz, Y. Laurent and J. A. Odriozola, Study of Aluminophosphate Oxynitride (AlPON) Materials by X-Ray Photoelectron (XPS) and Diffuse Reflectance Fourier Transform IR Spectroscopy (DRIFTS), *J. Mater. Chem.*, 1998, **8**(3), 687–691, DOI: **10.1039/A707222H**.

54 V. Lacivita, A. S. Westover, A. Kercher, N. D. Phillip, G. Yang, G. Veith, G. Ceder and N. J. Dudney, Resolving the Amorphous Structure of Lithium Phosphorus Oxynitride (Lipon), *J. Am. Chem. Soc.*, 2018, **140**(35), 11029–11038, DOI: **10.1021/jacs.8b05192**.

55 J. J. Yang, Y. Zhao and R. L. Frost, Infrared and Infrared Emission Spectroscopy of Gallium Oxide Alpha-GaO(OH) Nanostructures, *Spectrochim. Acta, Part A*, 2009, **74**(2), 398–403, DOI: **10.1016/j.saa.2009.06.032**.

56 J. M. Saniger, Al-O Infrared Vibrational Frequencies of γ-Alumina, *Mater. Lett.*, 1995, **22**(1), 109–113, DOI: **10.1016/0167-577X(94)00234-7**.